analytical chemistry

pubs.acs.org/ac Article

Electron−Ion Coupling for Nanostructured Photocathode in Ion-Assisted Photoelectrochemical Microfluidic Biosensing Platform

Dongquan Leng, Shixuan Wang, Tingting Wu, Xiang Ren, Yu Du,* Huangxian Ju, and Qin Wei*

Cite This: *Anal. Chem.* 2026, 98, 19314−19322 Read Online

ACCESS | Metrics & More | Article Recommendations | Supporting Information

ABSTRACT: The application of photocathodes in photoelectrochemical (PEC) devices is constrained by the low efficiency of light-induced electron−proton coupling and interfacial charge transfer. Herein, the nanoheterojunction structure formed by $BiFeO_3$ and CuO exhibits broad visible-light absorption and an adjustable photogenerated carrier separation potential. Based on this, we demonstrate that rapid ion adsorption in copper hexacyanoferrate (CuFe HCF)-modified cathode materials in the liquid phase can significantly enhance electron coupling efficiency. Precise modulation of the electron−ion receptor characteristics of the cathode materials enables targeted optimization of the coupling process, thereby improving the separation and transport efficiency of photogenerated charge carriers in the ion-assisted photoelectrochemical (IAPEC) system for the target recognition response. Furthermore, the incorporation of a microfluidic system physically isolates the automatic sampling recognition zone from the photoelectrochemical detection zone, fully exposing the active sites of the photoelectrochemical cathode material for detection. The IAPEC biosensing achieves highly efficient detection of the marine pollutant okadaic acid toxin, featuring a low detection limit of 23.1 pg/mL and a broad linear range of 0.1−200 ng/mL. This dual-engineering strategy not only overcomes the long-standing limitations of standard PEC systems but also establishes a foundational framework for designing efficient biosensors for marine environmental monitoring.

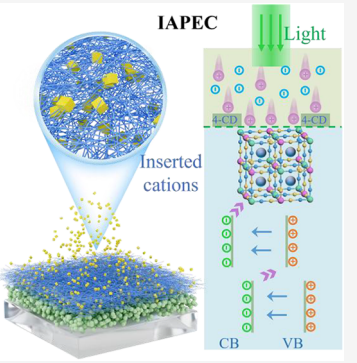

INTRODUCTION

In recent years, the interdisciplinary development of photoelectrochemical (PEC) and microfluidic technologies has opened new opportunities for designing efficient and sensitive biosensing platforms.[1−7] The core of PEC technology lies in the separation and transport of photogenerated charges, where the efficiency of electron−hole separation is a critical determinant of performance.[8−10] Traditional PEC systems are inherently limited by rapid recombination of photogenerated carriers and unfavorable charge-transfer kinetics at the interface, resulting in generally low energy conversion efficiency.[11,12] To address these challenges, researchers have focused on developing novel functional materials and innovative architectures to enhance carrier separation efficiency and interfacial charge-transfer rates.[13−16] For instance, the introduction of nanomaterials (e.g., graphene,[17] carbon nanotubes,[18] and metal−organic frameworks[19]) has been employed to improve charge separation efficiency, while strategies such as plasmonic resonance effects and electrochemical signal amplification have been utilized to enhance detection sensitivity.[20−23] These innovative studies provide new perspectives and directions for optimizing PEC-based biosensor performance.[24,25] Microfluidic systems, by precisely controlling sample delivery and reaction conditions, significantly improve the sensitivity and selectivity of analyte detection.[26,27] Consequently, advancements in microfluidic technology have provided critical support for enhancing the performance of PEC sensors.[28,29]

Prussian Blue Analogues (PBAs) are a class of functional materials characterized by three-dimensional open frameworks,[30,31] which have garnered significant attention due to their exceptional ionic intercalation properties and electrochemical performance.[32,33] The chemical composition of conventional PBAs is typically represented as $A_xM[Fe(CN)_6]_y\cdot(1-y)H_2O$, where iron and M are coordinated to six cyanide groups via Fe−C and M−N bonds, forming octahedral structures.[34] The three-dimensional open-framework structure of PBAs provides extensive pathways for ion migration, enabling rapid ion insertion and extraction.[35,36] This feature significantly enhances the charge storage capacity and electron transfer efficiency.[37] Counterions A and H_2O molecules occupy the internal spaces of the framework, transforming the open-framework lattice into cubic, monoclinic, rhombic, or triclinic structures.[38] The three-dimensional open-framework structure of these materials allows for the reversible insertion and extraction of ions such as H^+ and Na^+.[39] In the field of photocatalysis, PBAs have been successfully utilized as photoanode and photocathode

Received: May 8, 2026
Revised: May 29, 2026
Accepted: June 10, 2026
Published: June 22, 2026

https://doi.org/10.1021/acs.analchem.6c03166
Anal. Chem. 2026, 98, 19314−19322

Scheme 1. Okadaic Acid Detection in a Microfluidic Chip

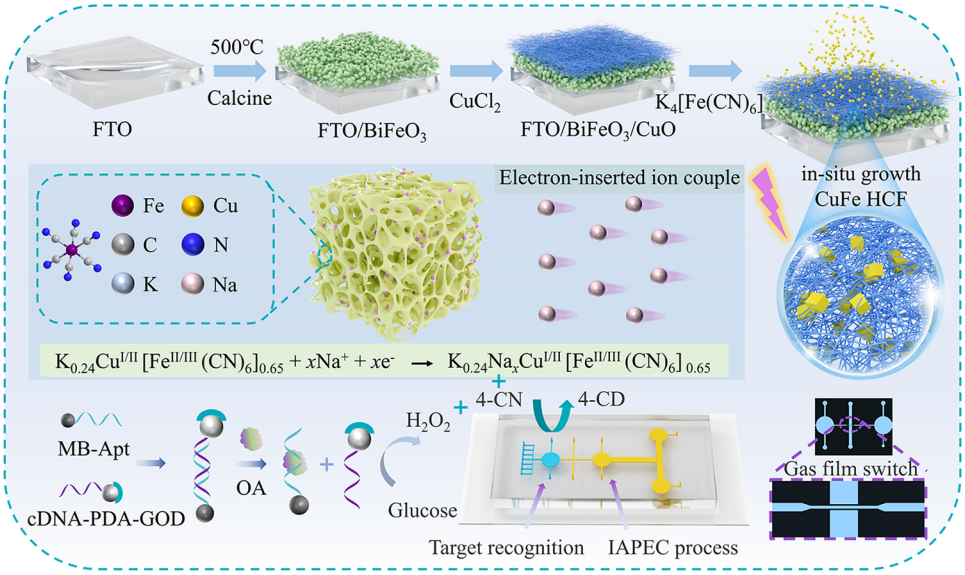

materials, with their ionic intercalation properties playing a critical role in enhancing light responsiveness and overall device performance.[40,41] The ability of PBAs to regulate electrode electronic properties through ionic intercalation makes them highly promising candidates for designing high-performance photocatalytic sensors. Notably, copper hexacyanoferrate (CuFe HCF) materials, which exhibit Cu^{+}/Cu^{2+} and Fe^{2+}/Fe^{3+} redox couples, demonstrate excellent electrochemical activity, effectively facilitating the transport and separation of photogenerated electrons.[42,43] This further highlights their potential for applications in PEC systems.

Bismuth-based semiconductor nanomaterial $BiFeO_3$ has become a research hotspot due to its suitable bandgap of ~2.2 eV, low toxicity, ease of synthesis, and high stability.[44,45] CuO, p-type semiconductor materials with a bandgap width of ~1.4 eV, exhibit excellent light absorption properties in the visible-light range.[46] The band structures enable the formation of effective charge transfer pathways in heterojunctions, facilitating the separation of photogenerated electron−hole pairs and thus offering potential for enhanced PEC conversion efficiency.[22] Based on these properties, this work developed an innovative ion-assisted PEC (IAPEC) microfluidic biosensing platform that fully leverages the superior characteristics of $BiFeO_3$/CuO composite materials and CuFe HCF. The ion-embedding property of CuFe HCF significantly enhances the electron−ion coupling effect, effectively promoting the separation of photogenerated electron−hole pairs in $BiFeO_3$/CuO and amplifying the PEC signal. Furthermore, CuFe HCF exhibits peroxidase-like nanoenzyme activity, enabling the catalytic conversion of hydrogen peroxide, released during the aptamer-based biorecognition process, with 4-chloro-1-naphthol (4-CN) to form precipitates on the photoelectrode surface. This process restricts the influence of ion diffusion on the electron−ion coupling process. By integrating microfluidic technology, the platform achieves precise control over analyte flow, further optimizing sensor performance. The innovative design of the electro-ion storage layer not only provides new insights into the design of high-performance photocatalytic materials and PEC-based biosensing platforms but also lays a foundation for their practical applications in biomedical diagnostics and environmental monitoring.

EXPERIMENTAL SECTION

Preparation of CuFe HCF and $BiFeO_3$/CuO/CuFe HCF

CuFe HCF was grown on the surface of $BiFeO_3$/CuO using the successive ionic layer adsorption and reaction (SILAR) method. First, the prepared $BiFeO_3$/CuO substrate material was immersed in a 1 mM $CuCl_2$ solution for 10 s. Subsequently, it was immersed in a 1 mM $K_4[Fe(CN)_6]$ solution for another 10 s. The CuFe HCF layer was formed on the surface of $BiFeO_3$/CuO. After repeating the above immersion process in the two solutions 5 times, the surface of the sample was rinsed with deionized water, and finally, the $BiFeO_3$/CuO/CuFe HCF composite material was obtained.

The synthesis of CuFe HCF was achieved by combining 20 mL of 5 mM $CuCl_2$ and $K_4[Fe(CN)_6]$, and continuously stirred at 30 °C for 2 h. Then, the reaction solution was centrifuged to separate the precipitate. The precipitate was alternately washed with ultrapure water and absolute ethanol by centrifugation 5 times. The resulting material was then subjected to vacuum desiccation at 60 °C to yield the final CuFe HCF product.

Procedure of Okadaic Acid Detection in a Microfluidic Chip

According to Scheme 1, on the prepared microfluidic chip, the gas-film switch was turned on to separate the PEC reaction zone from the target recognition zone. In the target recognition zone, 20 μL of magnetic beads-aptamer (MB-Apt), 20 μL of complementary DNA-polydopamine-glucose oxidase (cDNA-PDA-GOD), 20 μL of 0.1% bovine serum albumin (BSA), and 20 μL of okadaic acid (OA) at different concentrations were successively injected through different injection ports. Each step of the reaction was carried out under oscillation at 37 °C for 1 h. After the reaction, magnetic separation was performed on the reaction solution, and it was washed with PBS. Subsequently, 20 μL of 0.1 M glucose solution was added. After 30 min, the gas membrane was opened, and the solution was transferred to the PEC detection zone. During this period, 20 μL of 5 mM 4-CN was injected through the injection port. After 20 min, the solution was drained and washed. Finally, the air film switch was turned off to separate the target recognition from the PEC detection zone again. The microfluidic chip was positioned under a 100 mW/cm^2 LED light source for experimental analysis in a 0.16 M Na_2SO_4 solution at zero-bias conditions. The detailed structure diagram and physical image of the microfluidic chip are presented in Figure S1.

https://doi.org/10.1021/acs.analchem.6c03166
Anal. Chem. 2026, 98, 19314−19322

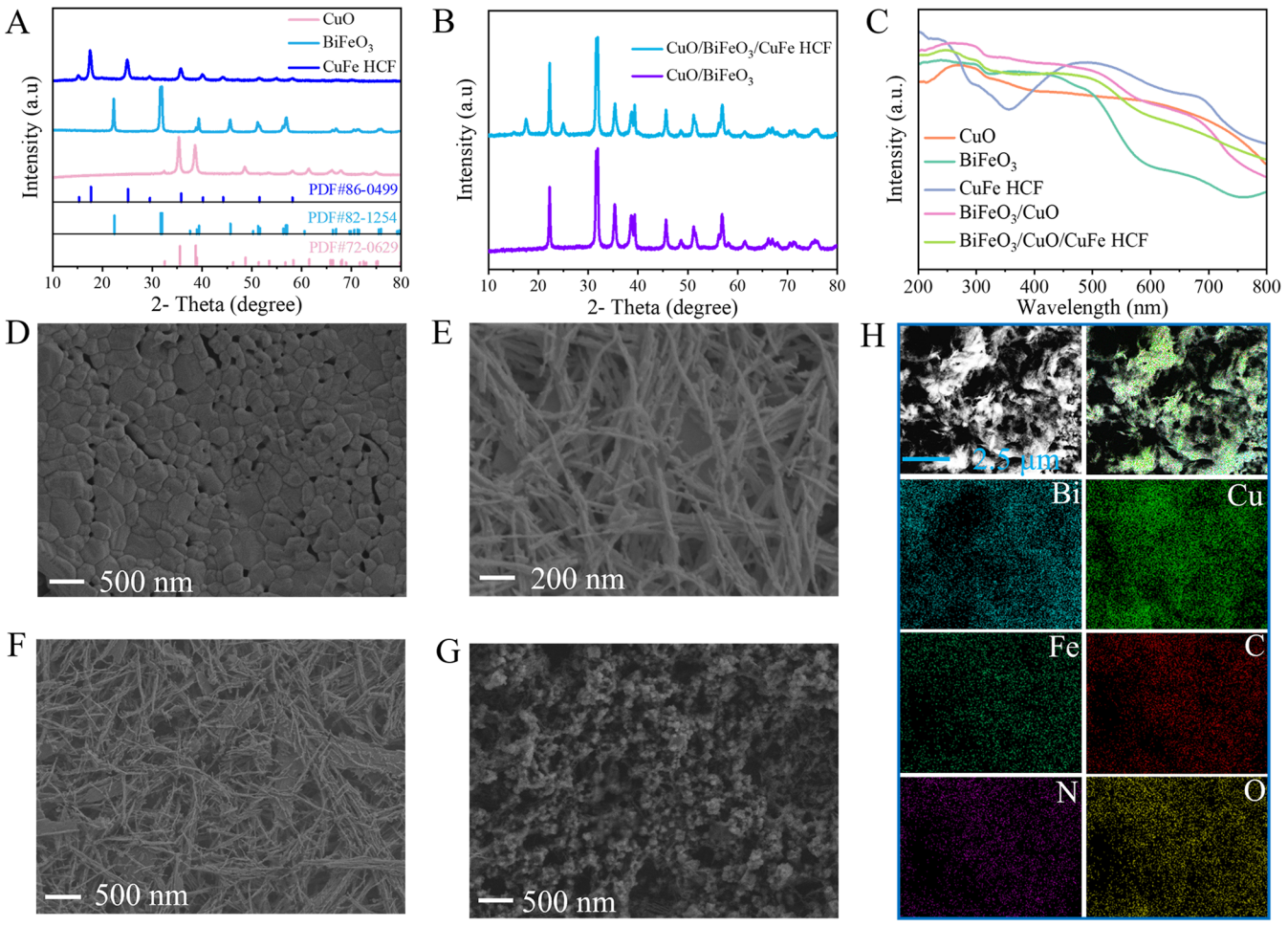

Figure 1. (A) XRD images of $BiFeO_3$, CuO, and CuFe HCF; (B) XRD images of $BiFeO_3$/CuO and $BiFeO_3$/CuO/CuFe HCF; (C) UV−vis image of $BiFeO_3$, CuO, CuFe HCF, $BiFeO_3$/CuO, and $BiFeO_3$/CuO/CuFe HCF; SEM images of (D) $BiFeO_3$, (E) CuO, (F) $BiFeO_3$/CuO, and (G) $BiFeO_3$/CuO/CuFe HCF; (H) SEM mappings of $BiFeO_3$/CuO/CuFe HCF.

RESULTS AND DISCUSSION

Characterization of Materials

A composite structure of $BiFeO_3$/CuO/CuFe HCF was prepared via the sol−gel method, hydrothermal, and SILAR method, as shown in Scheme 1. The crystal structures of $BiFeO_3$, CuO, CuFe HCF, and their composite were investigated by X-ray diffraction (XRD) analysis. The XRD pattern of the $BiFeO_3$ thin film exhibited characteristic peaks with lattice constants consistent with JCPDS card No. 82−1254 in Figure 1A. CuO showed distinct peaks at 35.5°, 38.7°, and 48.7°, corresponding to the (−111), (111), and (−202) planes of CuO, respectively, and its lattice constants matched JCPDS card No. 72−0629. CuFe HCF displayed diffraction peaks at 15.3°, 17.7°, 25.1°, and 35.8°, corresponding to the (111), (200), (220), and (400) planes of CuFe HCF in JCPDS card No. 86−0499, respectively. Furthermore, as depicted in Figure 1B, the diffraction patterns for both $BiFeO_3$/CuO and the $BiFeO_3$/CuO/CuFe HCF composite show no evidence of extraneous phases, indicating that the heterostructure had high purity and a well-defined crystal structure. The optical properties of $BiFeO_3$/CuO/CuFe HCF were studied using solid-state ultraviolet−visible (UV−vis) absorption spectroscopy. As shown in Figure 1C, $BiFeO_3$ exhibited strong absorption in the visible region (300−600 nm), with an absorption edge at 550 nm. CuO with an absorption edge above 800 nm showed absorption in the near-infrared region. CuFe HCF displayed absorption in the 500−700 nm region. The layered structure of the heterostructure enabled efficient light absorption across the entire spectrum from ultraviolet to near-infrared. The absorption range of the $BiFeO_3$/CuO/CuFe HCF composite structure was slightly smaller than that of the $BiFeO_3$/CuO heterojunction structure. The micromorphology of the materials was confirmed by scanning electron microscopy (SEM). As shown in Figure 1D, the surface of the deposited $BiFeO_3$ thin film had a dense and smooth structure. Figure 1E presents the structure of CuO nanowires, and Figure 1F shows the growth of CuO nanowires on the surface of the $BiFeO_3$ thin film. Figure 1G displays the structure after further growth of CuFe HCF on the surface of $BiFeO_3$/CuO by the SILAR method. The surface morphology and elemental composition of $BiFeO_3$/CuO/CuFe HCF were investigated by energy-dispersive spectroscopy (EDS). The EDS spectrum (Figure 1H) confirmed the presence of Bi, Fe, Cu, C, N, and O elements with a uniform elemental distribution, which verified the successful preparation. Furthermore, SEM and TEM results indicate that the PDA is uniformly sized nanospheres with a diameter of approximately 150 nm, providing the necessary conditions for the loading of Apt in Figure S2A,B.

The surface composition and chemical states of elements in the $BiFeO_3$/CuO/CuFe HCF composite material were

https://doi.org/10.1021/acs.analchem.6c03166
Anal. Chem. 2026, 98, 19314−19322

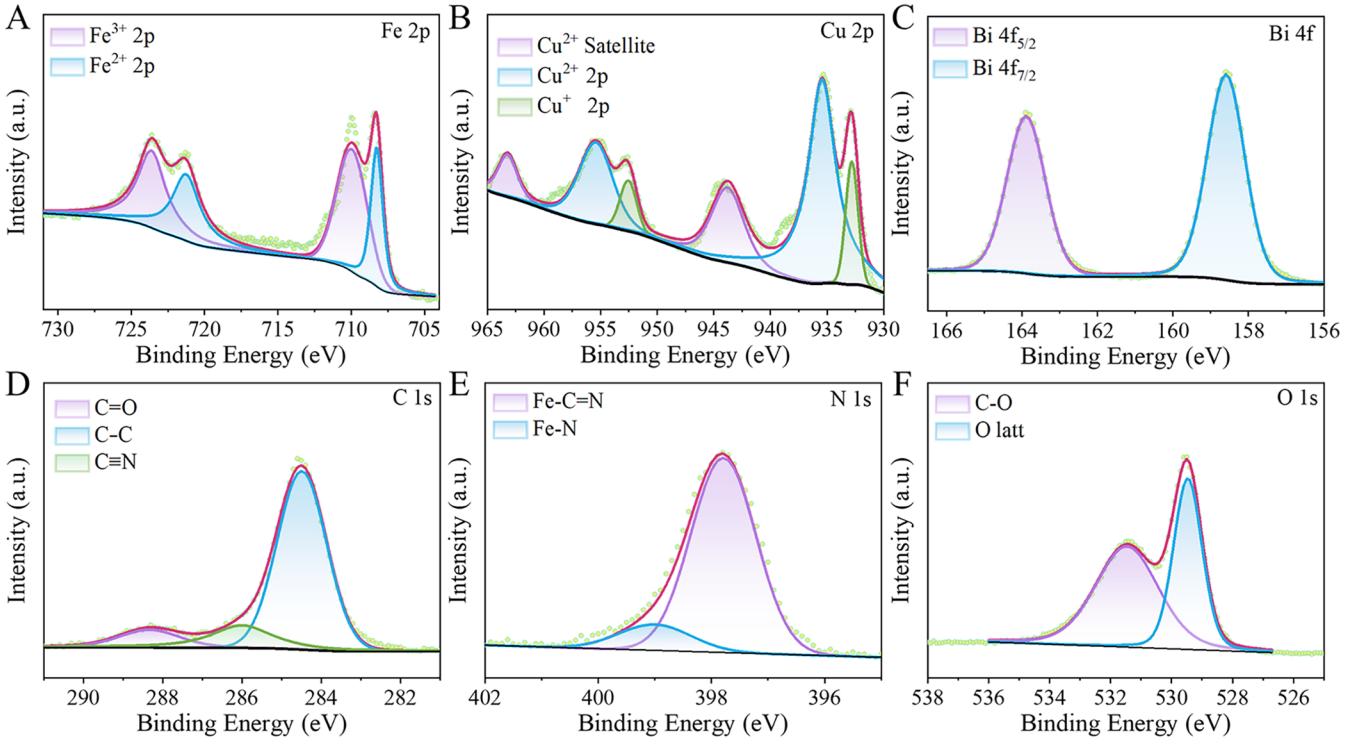

Figure 2. XPS spectra of (A) Fe 2p, (B) Cu 2p, (C) Bi 4f, (D) C 1s, (E) N 1s and (F) O 1s.

systematically analyzed using X-ray photoelectron spectroscopy (XPS) technology. The Fe 2p spectrum in Figure 2A shows two main peaks located at 710.0 and 723.7 eV, corresponding to the $2p_{3/2}$ and $2p_{1/2}$ energy levels of Fe^{3+} ions in $BiFeO_3$ and CuFe HCF, respectively. And the Fe 2p peaks are observed in the lower binding energy region (708.3 and 721.7 eV), confirming the existence of Fe^{2+} ions in CuFe HCF. Correspondingly, the Cu 2p spectrum illustrated in Figure 2B exhibits two characteristic peaks at 932.8 and 952.5 eV, which are assigned to the $2p_{3/2}$ and $2p_{1/2}$ transitions of monovalent Cu^+ ions, respectively. The peaks at 935.4 and 955.4 eV indicate the presence of Cu^{2+} ions. In addition, the satellite peaks in the higher binding energy region (943.8 and 963.2 eV) further confirm the presence of Cu^{2+} ions. The Bi 4f spectrum in Figure 2C shows two main peaks located at 163.8 and 158.5 eV, corresponding to the $4f_{5/2}$ and $4f_{7/2}$ energy levels of Bi^{3+} ions in $BiFeO_3$. The high-resolution C 1s spectrum shown in Figure 2D reveals three prominent peaks centered at 284.9, 285.9, and 288.4 eV, which represent the chemical states of C−C, C≡N, and C═O bonds. The N 1s spectrum in Figure 2E can be resolved into two characteristic peaks located at 397.8 eV (Fe−C≡N) and 399.1 eV (Fe−N). The O 1s spectrum presented in Figure 2F features a distinct peak at 529.5 eV, which is attributed to the presence of lattice oxygen. Meanwhile, the peak located at 531.5 eV is associated with the oxygen involved in C−O bonding. The XPS analysis confirms the successful incorporation of Fe, Cu, Bi, C, N, and O into the $BiFeO_3$/CuO/CuFe HCF composite.

PEC and IAPEC Process

The time-photocurrent intensity method was employed to evaluate the PEC and IAPEC processes of the photocathode in Figure 3A. The photocurrents of $BiFeO_3$ and CuFe HCF were weak, while the photocurrent of CuO was −5 μA. The photocurrent of the $BiFeO_3$/CuO heterojunction was higher than that of the single materials. After the growth of CuFe HCF on the surface of the $BiFeO_3$/CuO photoelectrode, the current intensity increased significantly, which confirmed that this composite structure was conducive to the effective separation of electrons and holes. The performance of the materials under dark and illumination conditions was tested by electrochemical impedance spectroscopy (EIS). Figure 3B shows that the EIS of $BiFeO_3$/CuO in the dark was lower than that of $BiFeO_3$, which proved the formation of the heterojunction. However, the EIS of $BiFeO_3$/CuO/CuFe HCF was higher than that of $BiFeO_3$/CuO, indicating that there was no effective charge transfer path between CuFe HCF and $BiFeO_3$/CuO in the dark. Under illumination, the EIS of $BiFeO_3$/CuO/CuFe HCF was significantly smaller than that of $BiFeO_3$/CuO and its own impedance in the dark, suggesting that it could form an efficient electron transfer path among the three components under illumination. The characterization of photocurrent intensity and electrochemical impedance preliminarily confirmed that in the $BiFeO_3$/CuO/CuFe HCF composite structure, the PEC process occurred in $BiFeO_3$/CuO, and the IAPEC process might occur in $BiFeO_3$/CuO/CuFe HCF. Therefore, the open-circuit voltage (OPV) of this process under illumination and different ion concentrations was further characterized in Figure 3C. The OPV of $BiFeO_3$/CuO in 0.2 M NaCl was similar to that in 0.05 M NaCl. The OPV of $BiFeO_3$/CuO/CuFe HCF in 0.2 M NaCl was higher than that in 0.05 M NaCl, which proved the influence of cation concentration on the IAPEC process. However, the photovoltages of $BiFeO_3$/CuO and $BiFeO_3$/CuO/CuFe HCF in 0.2 M $MgCl_2$ solution were lower than those in 0.2 M NaCl solution. This result indicates that ions with large radii have difficulty in ion intercalation. The schematic diagram of the crystal structure of CuFe HCF after Na^+ insertion is shown in Figure 3D. CuFe HCF features a rigid, three-dimensional face-centered cubic open-framework topology. In this crystalline

https://doi.org/10.1021/acs.analchem.6c03166
Anal. Chem. 2026, 98, 19314−19322

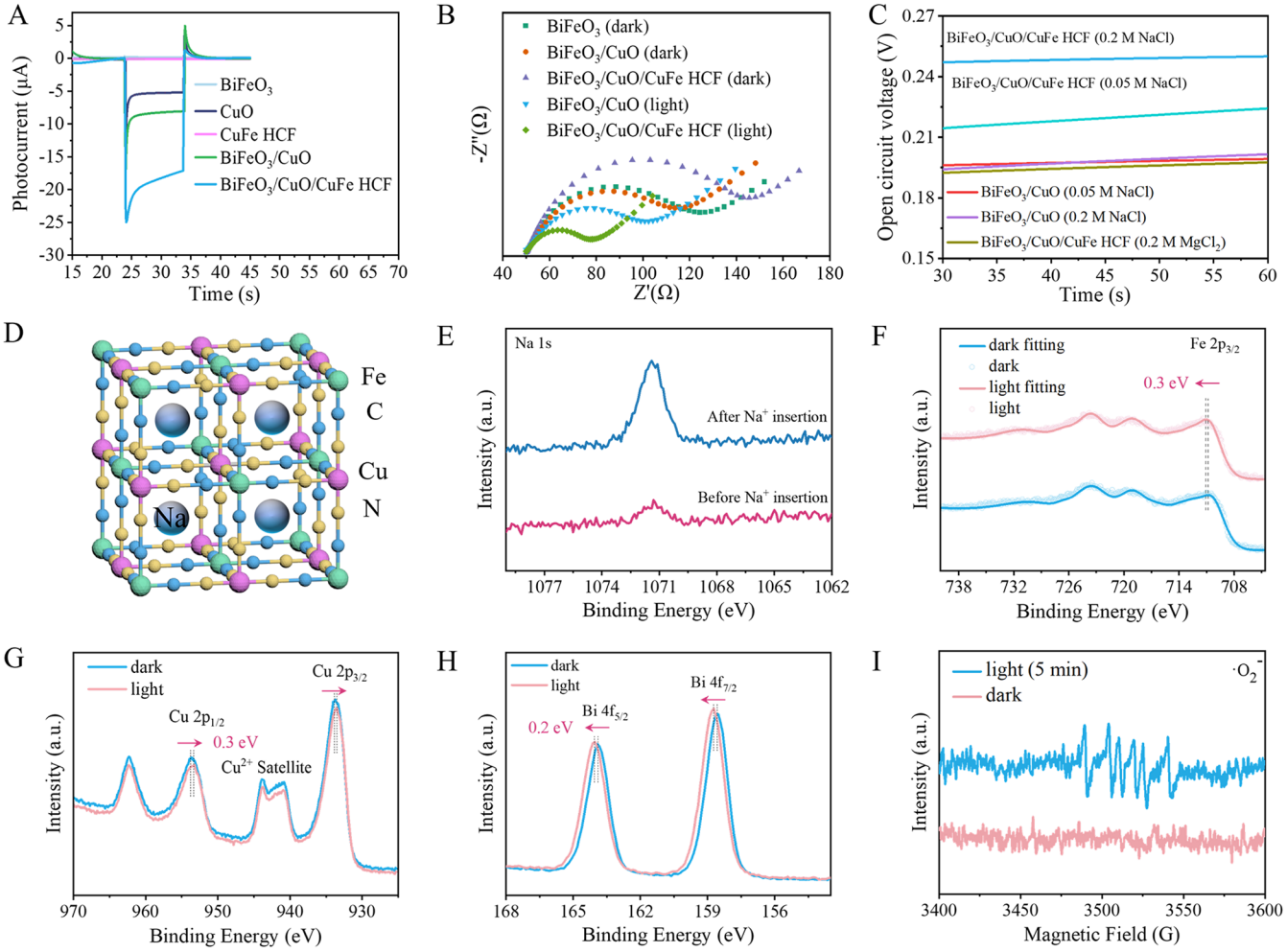

Figure 3. (A) PEC and IAPEC responses in 0.16 M Na_2SO_4 solution at 0 V; (B) EIS tests in the dark or under light irradiation in 5.0 mM $[Fe(CN)_6]^{3-/4-}$containing 0.1 M KCl; (C) OPV tests in different concentration solutions of ions; (D) schematic diagram of crystal structure of CuFe HCF after Na^+ insertion; (E) XPS spectra of Na 1s before and after Na^+ insertion; in situ XPS spectra of Fe 2p (F), Cu 2p (G), and Bi 4f (H) of $BiFeO_3$/CuO in the dark or under light irradiation and (I) ESR spectra of $BiFeO_3$/CuO in the dark or under light irradiation.

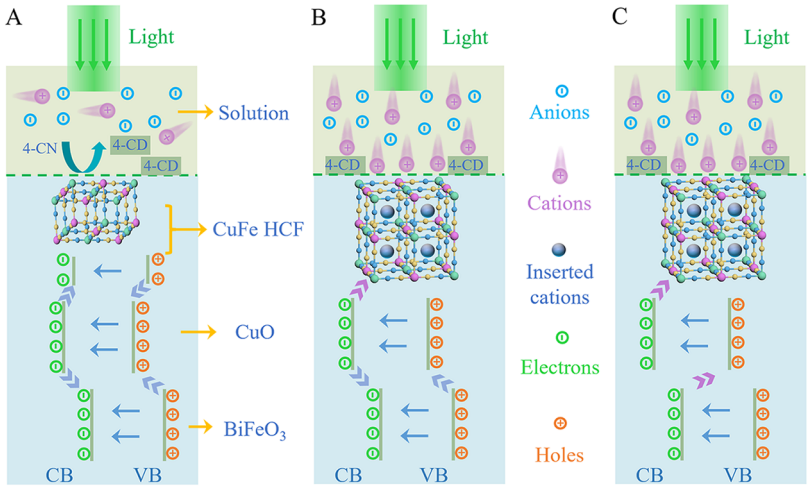

Figure 4. Mechanism of (A) PEC process, (B) IAPEC process of type-II heterojunction, and (C) IAPEC process of Z-scheme heterojunction.

matrix, transition metal nodes (Cu^{2+} and Fe^{3+}/Fe^{2+}) are precisely linked via bridging cyano (−C≡N−) ligands. This specific spatial arrangement yields highly ordered, spacious interstitial channels, creating optimal isotropic diffusion pathways that facilitate highly selective and reversible cation adsorption and intercalation. The high-resolution XPS spectra of the Na element in $BiFeO_3$/CuO/CuFe HCF before and after the reaction further confirmed the effective intercalation

https://doi.org/10.1021/acs.analchem.6c03166
Anal. Chem. 2026, 98, 19314−19322

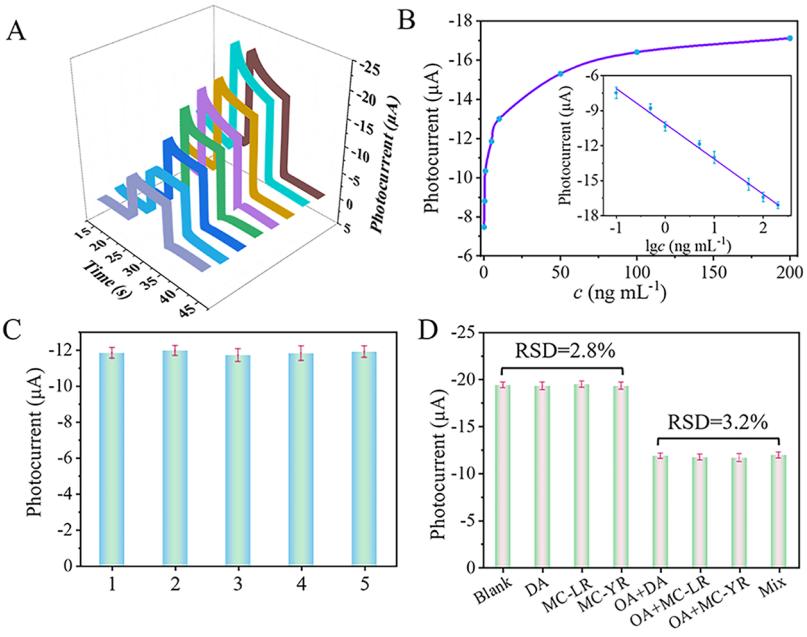

Figure 5. (A) PEC response in 0.16 M Na_2SO_4 solution at 0 V (0.1, 0.5, 1, 5, 10, 50, 100, and 200 ng/mL); (B) the corresponding calibration curve of OA detection; (C) reproducibility test in 0.16 M Na_2SO_4 solution (c = 5 ng/mL); and (D) selectivity test in 0.16 M Na_2SO_4 solution (c = 5 ng/mL). Error bars = SD (n = 3).

of Na^+ ions after illumination in Figure 3E. In contrast, as shown in Figure S3, there was no obvious change in the state of K^+ ions before and after the reaction.

Possible Mechanisms and Feasibility Analysis

An in-depth investigation was conducted to elucidate the possible mechanism of the PEC and IAPEC processes. Through quantitative bandgap analysis using the Tauc equation, the intrinsic bandgaps of $BiFeO_3$, CuO, and CuFe HCF were determined to be 2.26, 1.43, and 1.88 eV, respectively (Figure S4). The calculation of valence band (VB) positions was based on VB-XPS data, employing the formula: $E_{VB} = \varphi + E_{VB}$, XPS −4.44, where φ represents the work function of the XPS instrument (4.8 eV), and 4.44 eV corresponds to the constant work function difference between the vacuum potential and the standard hydrogen electrode at pH = 0.[47] The XPS spectra shown in Figure S5 reveal that the valence bands of $BiFeO_3$ (+2.26 eV), CuO (+0.72 eV), and CuFe HCF (+1.42 eV) exhibit an interlaced band displacement characteristic. By applying the fundamental relationship $E_{CB} = E_{VB} - E_g$, the conduction band (E_{CB}) positions were pinpointed at 0.00 eV for $BiFeO_3$, −0.71 eV for CuO, and −0.46 eV for CuFe HCF. Electron spin resonance (ESR) analysis detected the

DMPO (5,5-dimethyl-1-pyrrolidin-N-oxide) $^{\bullet}OH^-$ signal in CuFe HCF in ultrapure water (UP) containing H_2O_2 (Figure S6), confirming its peroxidase-like activity.[48,49] Based on the above analysis, it can be clearly determined that there are three electron transfer pathways and their corresponding detection mechanisms in the $BiFeO_3$/CuO heterojunction. Through in-depth research, the IAPEC process rules out the possibility of the band-mismatched PEC process shown in Figure 4A. Further in situ XPS analysis reveals changes in the binding energies of various elements in the $BiFeO_3$/CuO heterojunction under light illumination. Specifically, the binding energy of Fe $2p_{3/2}$ increases by 0.3 eV in Figure 3F, that of Cu $2p_{3/2}$ decreases by 0.3 eV in Figure 3G, and that of Bi $4f_{5/2}$ increases by 0.2 eV in Figure 3H. This phenomenon indicates that electrons in $BiFeO_3$ migrate toward CuO under light illumination. Combining with this experimental result, the possibility of the type-II heterojunction shown in Figure 4B can be excluded. In addition, the ESR test results show that no DMPO-$^{\bullet}O_2^-$ signal is detected in the $BiFeO_3$/CuO heterojunction under dark conditions (as shown in Figure 3I). After 5 min of light illumination, an obvious signal of the DMPO-$^{\bullet}O_2^-$ adduct appears. This result further confirms that the $BiFeO_3$/CuO heterojunction is a Z-scheme heterojunction. Therefore, the IAPEC detection process is as follows: Under light illumination, electrons in the VB of $BiFeO_3$ and CuO are excited to the conduction bands. The electrons in the conduction band of $BiFeO_3$ migrate to CuO, and the photogenerated electrons in the conduction band of CuO migrate to CuFe HCF. Simultaneously, Na^+ ions are inserted into the interior to achieve charge balance. This process enables the efficient separation of electrons and holes in Figure 4C. After the target biomolecule recognition process, glucose oxidase decomposes glucose to generate H_2O_2. The addition of 4-CN leads to the formation of an insoluble precipitate, 4-CD, on the electrode surface under the catalytic action of CuFe HCF. This precipitate hinders the insertion of ions into the interior of CuFe HCF. The change in photocurrent realizes the detection of the target concentration.

OA Analysis

OA, a toxin widely present in the marine environment, exhibits significant bioaccumulation characteristics. Ingesting an excessive amount of OA can cause damage to multiple vital systems in the human body, such as the nervous system and the digestive system. On the basis of this, the IAPEC sensor was designed and constructed for the efficient and sensitive detection of OA. When preparing CuFe HCF via the SILAR method, the optimal conditions (the number of cycles was 5) were determined through experimental optimization in Figure S7A. Additionally, the concentration of the Na^+ electrolyte

https://doi.org/10.1021/acs.analchem.6c03166
Anal. Chem. 2026, 98, 19314−19322

used in the photocurrent test was 0.16 mol/L, as shown in Figure S7B. In the detection system of this sensor, the different concentrations of OA present in the detection sample affect the IAPEC processes. The results shown in Figure 5A demonstrate the feasibility of this strategy. The plotted corresponding standard curve (Figure 5B) results show that in the range of 0.1 ng/mL to 200 ng/mL, there is a linear relationship between the logarithm of the OA concentration and the photocurrent (I). The obtained linear regression equation is $I = -3.02 \lg c - 10.12$ ($R^2 = 0.992$), and the limit of detection (LOD) can be as low as 23.1 pg/mL (S/N = 3). To verify the advantages of this sensor, we compared it with several commonly used OA detection methods, including surface-enhanced Raman scattering sensors, electrochemical sensors, electrochemiluminescence sensors, and fluorescence sensors (Table S1). The comparison results show that the IAPEC sensor in this study has a wider detection range and a lower LOD. This indicates that this sensor has great potential in practical applications and is expected to become an effective tool for the rapid and accurate detection of OA.

Performance Analysis of the IAPEC Biosensor

To evaluate the reproducibility of the sensors, we selected sensors from different batches to detect OA at a concentration of 5 ng/mL. The detection results are shown in Figure 5C. The IAPEC responses of sensors from each batch toward the target analyte at the same concentration were consistent, and the relative standard deviations (RSDs) were all controlled within 3.5%. This result indicates that the sensors possess good reproducibility. Considering the complex and diverse composition of the marine environment, this study used the proposed method to conduct a specificity analysis on interferents at a concentration of 10 ng/mL (present individually or mixed with 5 ng/mL of OA), including microcystin-LR (MC-LR), domoic acid (DA), and microcystin-YR (MC-YR) as target analytes. As can be seen from Figure 5D, when the interferents were used as target analytes alone, their signals were similar to the IAPEC intensity of the blank samples, and the RSD of the four groups of data was 2.8%. When OA was mixed with any one of the interferents or with all of the interferents, the RSD of the IAPEC intensity was 3.2%. This result demonstrates that the proposed method has the ability to resist interference from the complex samples.

Serum Sample Analysis

Polluted scallop samples were selected as research objects. High-performance liquid chromatography (HPLC) was utilized to quantify the original level of the target analyte, which was found to be 12.58 ng/mL. Meanwhile, the IAPEC method was used for simultaneous determination, and the measured value was 12.75 ng/mL. This result indicates that there is no significant difference between the two methods in the measurement results, suggesting that the IAPEC method has a certain degree of accuracy. Then, three different concentrations of OA solutions (5.00 ng/mL, 8.00 ng/mL, and 12.00 ng/mL) were added to the original samples, respectively. Subsequently, the samples after the addition of the standard solutions were measured by the IAPEC method. The results showed that the recovery rate of OA ranged from 96.1% to 103.7%, and the relative standard deviation of the detected values was less than 4.3%, as shown in Table S2. These data and phenomena confirm that the proposed IAPEC method has broad and promising application potential in relevant fields.

CONCLUSION

In summary, this study presents an innovative methodology that leverages ion-assisted nanomaterial engineering to overcome the inherent challenges associated with traditional photocathode materials. By integrating CuFe HCF as a cathode modifier with exceptional ion adsorption, the photoinduced electron−hole coupling efficiency in $BiFeO_3$/CuO heterostructures has been significantly changed. The incorporation of a microfluidic system ensures precise spatial segregation between the sampling recognition and detection zones, thereby maximizing the exposure of active sites on the cathode material and improving the detection accuracy. This dual-engineering strategy not only transcends the limitations of conventional PEC systems but also offers a universal solution for designing high-performance biosensors tailored to marine environmental monitoring.

ASSOCIATED CONTENT

Supporting Information

The Supporting Information is available free of charge at https://pubs.acs.org/doi/10.1021/acs.analchem.6c03166.

Materials and reagents, apparatus, preparation of materials, and other details, along with recovery experiments in the scallop sample (PDF)

AUTHOR INFORMATION

Corresponding Authors

Yu Du − *School of Water Conservancy and Environment, University of Jinan, Jinan 250022, P. R. China;* orcid.org/0000-0002-9002-8845; Email: duyu_ujn@163.com

Qin Wei − *Collaborative Innovation Center for Green Chemical Manufacturing and Accurate Detection; Key Laboratory of Interfacial Reaction & Sensing Analysis in Universities of Shandong, School of Chemistry and Chemical Engineering, University of Jinan, Jinan 250022, P. R. China; Department of Chemistry, Sungkyunkwan University, Suwon 16419, Republic of Korea; College of Pharmacy, Dali University, Yunnan 671000, P. R. China;* orcid.org/0000-0002-3034-8046; Email: sdjndxwq@163.com

Authors

Dongquan Leng − *Collaborative Innovation Center for Green Chemical Manufacturing and Accurate Detection; Key Laboratory of Interfacial Reaction & Sensing Analysis in Universities of Shandong, School of Chemistry and Chemical Engineering, University of Jinan, Jinan 250022, P. R. China*

Shixuan Wang − *Collaborative Innovation Center for Green Chemical Manufacturing and Accurate Detection; Key Laboratory of Interfacial Reaction & Sensing Analysis in Universities of Shandong, School of Chemistry and Chemical Engineering, University of Jinan, Jinan 250022, P. R. China*

Tingting Wu − *Collaborative Innovation Center for Green Chemical Manufacturing and Accurate Detection; Key Laboratory of Interfacial Reaction & Sensing Analysis in Universities of Shandong, School of Chemistry and Chemical Engineering, University of Jinan, Jinan 250022, P. R. China*

Xiang Ren − *Collaborative Innovation Center for Green Chemical Manufacturing and Accurate Detection; Key Laboratory of Interfacial Reaction & Sensing Analysis in Universities of Shandong, School of Chemistry and Chemical*

https://doi.org/10.1021/acs.analchem.6c03166
Anal. Chem. 2026, 98, 19314−19322

Engineering, University of Jinan, Jinan 250022, P. R. China; orcid.org/0000-0002-4321-4282

Huangxian Ju − *Collaborative Innovation Center for Green Chemical Manufacturing and Accurate Detection; Key Laboratory of Interfacial Reaction & Sensing Analysis in Universities of Shandong, School of Chemistry and Chemical Engineering, University of Jinan, Jinan 250022, P. R. China; State Key Laboratory of Analytical Chemistry for Life Science, Department of Chemistry, Nanjing University, Nanjing 210023, P. R. China;* orcid.org/0000-0002-6741-5302

Complete contact information is available at: https://pubs.acs.org/10.1021/acs.analchem.6c03166

Notes

The authors declare no competing financial interest.

■ ACKNOWLEDGMENTS

This study was supported by the National Natural Science Foundation of China (Nos. 22574062, 22574063, 22274062, 22511540056), Shandong Province Science and Technology Small and Medium Enterprises Innovation Ability Enhancement Project (2025TSGCCZZB0987), Jinan University and Institute Innovation Team Project (202534040), and Yunnan Provincial Science and Technology Plan Project (202405AF140007). The authors would like to thank Scientific Compass (www.shiyanjia com) for the support of XPS analysis.

■ REFERENCES

(1) Ibrahim, O. A.; Navarro-Segarra, M.; Sadeghi, P.; Sabaté, N.; Esquivel, J. P.; Kjeang, E. Microfluidics for Electrochemical Energy Conversion. *Chem. Rev.* **2022**, *122* (7), 7236−7266.

(2) Fattahi, Z.; Hasanzadeh, M. Nanotechnology-assisted microfluidic systems for chemical sensing, biosensing, and bioanalysis. *TrAC Trends Anal. Chem.* **2022**, *152*, No. 116637.

(3) Chen, Y.; Zhang, J.; Li, X.; Liu, T.; Feng, J.; Jiang, W.; Song, X. Novel Benzopyran-Coumarin Derivative-Sensitized BiOI Nanoarray-Driven Photoelectrochemical/Fluorescence Dual-Mode Microfluidic Biosensor for Sensitive Detection of Golgi Protein 73. *ACS Sens.* **2025**, *10*, 8342−8350, DOI: 10.1021/acssensors.5c01394.

(4) Du, Y.; Geng, H.; Chen, J.; Sun, X.; Wu, T.; Ma, H.; Gao, Z.; Wei, Q. Cascade Catalytic Iron Phosphate Nanozyme-Driven Signal Amplification in S-Scheme AgBr/La-BiOBr-OV for Sensitive Dual-Channel Microfluidic PEC Detection of CA15−3 and CA125. *Anal. Chem.* **2025**, *97* (30), 16611−16618.

(5) Niu, X.; Lu, C.; Su, D.; Wang, F.; Tan, W.; Qu, F. Construction of a Polarity-Switchable Photoelectrochemical Biosensor for Ultrasensitive Detection of miRNA-141. *Anal. Chem.* **2021**, *93* (40), 13727−13733.

(6) Kong, W.; Xiang, M.-H.; Xia, L.; Zhang, M.; Kong, R.-M.; Qu, F. In-situ synthesis of 3D Cu2O@Cu-based MOF nanobelt arrays with improved conductivity for sensitive photoelectrochemical detection of vascular endothelial growth factor 165. *Biosens. Bioelectron.* **2020**, *167*, No. 112481.

(7) Niu, X.; Zhao, Y.; Wang, F.; Wu, J.; Qu, F.; Tan, W. Ultrasensitive Photoelectrochemical Biosensor Based on Novel Z-Scheme Heterojunctions of Zn-Defective CdS/ZnS for MicroRNA Assay. *Anal. Chem.* **2021**, *93* (51), 17134−17140.

(8) Kong, W.; Zhu, D.; Zhang, Y.; Luo, R.; Ma, J.; Lei, J.; Ju, H. Electron Donor Coordinated Metal-Organic Framework to Enhance Photoelectrochemical Performance. *Angew. Chem., Int. Ed.* **2023**, *62* (33), No. e202308514.

(9) Wang, Q.; Oldham, L. I.; Giner-Requena, A.; Wang, Z.; Benetti, D.; Montilla-Verdú, S.; Chen, R.; Du, D.; Lana-Villarreal, T.; Aschauer, U.; et al. Enhancing Photoelectrochemical Water Oxidation Using Ferromagnetic Materials and Magnetic Fields. *J. Am. Chem. Soc.* **2024**, *146* (50), 34681−34689.

(10) Zhang, C.; Wang, Y.; Sun, W.; Hua, Z.; Zhang, Z.; Gong, S.; Wang, D.; Tian, Y. Tailoring Non-Covalent Interaction Via Single Atom to Boost Interfacial Charge Transfer Toward Photoelectrochemical Water Oxidation. *Adv. Mater.* **2025**, *37* (4), No. 2410632.

(11) Cai, B.; Pavliuk, M. V.; Berggren, G.; Tian, H. Bio-hybrid photoelectrochemical catalysis for solar fuels and chemicals conversion. *Nat. Commun.* **2025**, *16* (1), No. 9131.

(12) Zhou, S.; Sun, K.; Satriyatama, A.; Facchinetti, I.; Toe, C. Y.; Hao, X.; Amal, R. Nanoengineered Kesterite Photocathodes: Enhancing Photoelectrochemical Performance for Water Splitting and Beyond. *ACS Nano* **2025**, *19* (18), 17041−17061.

(13) Wang, J.; Liu, K.; Liao, W.; Kang, Y.; Xiao, H.; Chen, Y.; Wang, Q.; Luo, T.; Chen, J.; Li, H.; et al. Metal vacancies in semiconductor oxides enhance hole mobility for efficient photoelectrochemical water splitting. *Nat, Catal.* **2025**, *8* (3), 229−238.

(14) Kong, W.; Liu, T.; Meng, X.; Dong, P.; Lei, J.; Ju, H. Intrareticular Energy Transfer in Dual-Photosensitized Metal−Organic Frameworks to Enhance Photoelectrochemical Performance. *J. Am. Chem. Soc.* **2025**, *147* (28), 24976−24983.

(15) Jin, W.; Go, H.; Jeong, J.; Park, J.; Tayyebi, A.; Yu, J. M.; Kim, S.; Choi, K.; Jang, J.-W.; Seo, K. Nickel Hydroxide Catalyzed Bias-free Photoelectrochemical NH3 Production via Nitrate Reduction. *Adv. Mater.* **2025**, *37* (38), No. 2506567.

(16) Si, S.; Mao, Y.; Liu, Y.-A.; Ma, J.; Jiang, W.; Zhao, E.-D.; Song, K.; Cheng, H.; Huang, B.; Liu, D.; Xiong, Y. Selective photoelectrochemical synthesis of adipic acid using single-atom Ir decorated α-Fe2O3 photoanode. *Nat. Commun.* **2025**, *16* (1), No. 5128.

(17) Wei, Z.; Su, Y.; Pan, W.; Shen, J.; Fan, R.; Yang, W.; Deng, Z.; Shen, M.; Peng, Y. Covalently Grafting Graphene onto Si Photocathode to Expedite Aqueous Photoelectrochemical CO2 Reduction. *Angew. Chem., Int. Ed.* **2023**, *62* (28), No. e202305558.

(18) Sun, X.; Chen, J.; Zhai, J.; Zhang, H.; Dong, S. Beyond Photosynthesis: H2O/H2O2/O2 Self-Circulation-Based Biohybrid Photoelectrochemical Cells for Direct and Sustainable Solar-to-Fuel-to-Electric Power Conversion. *J. Am. Chem. Soc.* **2022**, *144* (50), 23073−23080.

(19) Wang, C.-S.; Jiang, Y.; Li, Z.; Kong, F.-Y.; Wang, W.; Zhao, W.-W. Graphene Photoelectrochemical Transistor for Dual-Directional Signal-on Biosensing. *Adv. Funct. Mater.* **2025**, *35* (30), No. 2500235.

(20) Zhao, C.-Q.; Zhou, J.; Wu, K.-W.; Ding, S.-N.; Xu, J.-J.; Chen, H.-Y. Plasmonic Enhanced Gold Nanoclusters-Based Photoelectrochemical Biosensor for Sensitive Alkaline Phosphatase Activity Analysis. *Anal. Chem.* **2020**, *92* (10), 6886−6892.

(21) Xu, J.; Deng, H.; Xiao, Y.; Yuan, R.; Chai, Y. A methylene blue dye/Ru(bpy)3Cl2 co-sensitized H3BTTC structure with high photoelectric conversion efficiency for ultrasensitive detection of breast cancer biomarker. *Biosens. Bioelectron.* **2026**, *294*, No. 118170.

(22) Qin, J.; Wu, D.; Yu, Z.; Tang, D. Modulating Built-In Electric Field Strength in an In2S3/CdS Heterojunction via Vanadium Doping for a Photoelectrochemical Immunoassay. *Anal. Chem.* **2025**, *97* (42), 23631−23639.

(23) Ju, P.; Wang, Z.; Xu, B.; Chi, J.; Wang, F.; Zheng, M.; Liu, Q.; Wang, L. Ultrasensitive Porphyrin Organic Semiconductor-Sensitized CdS-Gated Organic Photoelectrochemical Transistor Biosensor for Rapid Detection of Tobramycin. *Anal. Chem.* **2025**, *97* (40), 22299−22307.

(24) Gao, Y.; Li, M.; Zeng, Y.; Liu, X.; Tang, D. Tunable Competitive Absorption-Induced Signal-On Photoelectrochemical Immunoassay for Cardiac Troponin I Based on Z-Scheme Metal−Organic Framework Heterojunctions. *Anal. Chem.* **2022**, *94* (39), 13582−13589.

(25) Cai, G.; Yu, Z.; Ren, R.; Tang, D. Exciton−Plasmon Interaction between AuNPs/Graphene Nanohybrids and CdS Quantum Dots/TiO2 for Photoelectrochemical Aptasensing of Prostate-Specific Antigen. *ACS Sensors* **2018**, *3* (3), 632−639.

(26) Gao, D.; Ma, Z.; Jiang, Y. Recent advances in microfluidic devices for foodborne pathogens detection. *TrAC Trends Anal. Chem.* **2022**, *157*, No. 116788.
(27) Hou, Y.; Liu, Z.; Huang, H.; Lou, C.; Sun, Z.; Liu, X.; Pang, J.; Ge, S.; Wang, Z.; Zhou, W.; Liu, H. Biosensor-Based Microfluidic Platforms for Rapid Clinical Detection of Pathogenic Bacteria. *Adv. Funct. Mater.* **2025**, *35* (1), No. 2411484.
(28) Zhou, Q.; Lin, Y.; Zhang, K.; Li, M.; Tang, D. Reduced graphene oxide/BiFeO3 nanohybrids-based signal-on photoelectrochemical sensing system for prostate-specific antigen detection coupling with magnetic microfluidic device. *Biosens. Bioelectron.* **2018**, *101*, 146−152.
(29) Shu, J.; Tang, D. Recent Advances in Photoelectrochemical Sensing: From Engineered Photoactive Materials to Sensing Devices and Detection Modes. *Anal. Chem.* **2020**, *92* (1), 363−377.
(30) Lao, S.; Gao, F.; Yu, Z.; Xu, M.; Sheng, E.; Tie, D.; He, Y.; Tang, D. Partially Phosphidated Prussian Blue Analogues Derived Heterostructure Nanozyme for Colorimetric-Photothermal Dual-Mode Immunoassay. *Anal. Chem.* **2026**, *98* (15), 11384−11392.
(31) Lao, S.; Wang, H.; Wu, D.; Wei, Q.; Tang, D. Dual-metal CuFe/Fe cube nanozyme with Prussian blue analogue for highly efficient colorimetric immunoassay. *Biosens. Bioelectron.* **2025**, *287*, No. 117689.
(32) Zhang, H.; Li, J.; Liu, J.; Gao, Y.; Fan, Y.; Liu, X.; Guo, C.; Liu, H.; Chen, X.; Wu, X.; et al. Understanding capacity fading from structural degradation in Prussian blue analogues for wide-temperature sodium-ion cylindrical battery. *Nat. Commun.* **2025**, *16* (1), No. 2520.
(33) He, Y.; Dreyer, S. L.; Akçay, T.; Diemant, T.; Mönig, R.; Ma, Y.; Tang, Y.; Wang, H.; Lin, J.; Schweidler, S.; et al. Leveraging Entropy and Crystal Structure Engineering in Prussian Blue Analogue Cathodes for Advancing Sodium-Ion Batteries. *ACS Nano* **2024**, *18* (35), 24441−24457.
(34) Huang, Y.; Gong, W.; Zhang, G.; Li, Z.; Lin, H.; Yan, Q.; Ren, S. Dimensional Transformation of Molecular Magnetic Materials. *ACS Nano* **2022**, *16* (8), 13232−13240.
(35) Shen, Y.; Zou, J.; Lan, H.; Ding, Y.; Liang, Z.; Yang, Z.; Zeng, Z.; Long, J.; Zhao, Y.; Fu, L.; Zeng, M. Unlocking Prussian Blue Analogues Inert-Site to Achieve High-Capacity Ammonium Storage. *Adv. Funct. Mater.* **2024**, *34* (29), No. 2400598.
(36) Shu, W.; Han, C.; Wang, X. Prussian Blue Analogues Cathodes for Nonaqueous Potassium-Ion Batteries: Past, Present, and Future. *Adv. Funct. Mater.* **2024**, *34* (1), No. 2309636.
(37) Chen, Z.; Zhang, Y.; Li, F.; Wei, K.; Tang, H.; Wei, S.; Jiang, Y.; Feng, Q.; Gong, K. Decoding intercalation-chemistry discrepancies to couple alkali cations with Prussian blue analogue cathodes. *Nano Energy* **2025**, *141*, No. 111097.
(38) Camacho, P. S.; Wernert, R.; Duttine, M.; Wattiaux, A.; Rudola, A.; Balaya, P.; Fauth, F.; Berthelot, R.; Monconduit, L.; Carlier, D.; Croguennec, L. Impact of Synthesis Conditions in Na-Rich Prussian Blue Analogues. *ACS Appl. Mater. Interfaces* **2021**, *13* (36), 42682−42692.
(39) Zhou, B.; Gao, Y.; Lin, X.; Yang, B.; Kang, N.; Qiao, Y.; Zhang, H.; Li, L.; Chou, S. Bulk and interface engineering of Prussian blue analogue cathodes for high-performance sodium-ion batteries. *Chem. Sci.* **2025**, *16* (30), 13594−13628.
(40) Yang, B.; Zhang, X.; Jin, F.; Ma, X.; Li, Y.; Jin, Z. Novel strategy of in situ growth of a prussian blue analogue on Zn2In2S5 Nanoflower balls in concert with interfacial electron-directional transfer boosting photocatalytic hydrogen production. *J. Power Sources* **2025**, *657*, No. 238194.
(41) Lin, J.; Han, X.; Liu, S.; Lv, Y.; Li, X.; Zhao, Y.; Li, Y.; Wang, L.; Zhu, S. Nitrogen-doped cobalt-iron oxide cocatalyst boosting photoelectrochemical water splitting of BiVO4 photoanodes. *Appl. Catal., B* **2023**, *320*, No. 121947.
(42) Zhao, X.; Liu, N.; Zheng, M.; Wang, X.; Xu, Y.; Liu, J.; Li, F.; Wang, L. Four-Electron Redox Reaction in Prussian Blue Analogue Cathode Material for High-Performance Sodium-Ion Batteries. *ACS Energy Letters* **2024**, *9* (6), 2748−2757.
(43) Luo, S.; Chen, W.; Wang, Y.; Hu, W.; Xiao, W.; Wu, J.; Ju, H. Transforming Chemiluminescence from Flash to Glow by Breaking the Catalytic Limitation with a Medium-Entropy Nanozyme. *Angew. Chem., Int. Ed.* **2025**, *64* (39), No. e202503734.
(44) Seo, D.; Grieder, A.; Radmilovic, A.; Alamudun, S. F.; Yuan, X.; Ping, Y.; Choi, K.-S. Atomic doping to enhance the p-type behavior of BiFeO3 photoelectrodes for solar H2O2 production. *J. Mater. Chem. A* **2024**, *12* (31), 20437−20448.
(45) Ajay; Saroha, J.; Ingole, P. P. A changeable critical state for a switchable photocurrent direction via the photo-electrochemical photocurrent polarity switching effect in BiFeO3 nanoparticulate films. *Chem. Sci.* **2024**, *15* (42), 17372−17379.
(46) Geng, W.; Liu, H.; Yuan, X.; Ji, J.; Yan, Z.; Yang, R. 1D/3D MOF-919-Sc Networked Octahedron-Derived 2D/3D Sc2O3@CuO Layered Octahedron for Polarity-Switchable Photoelectrochemical Sensing. *Anal. Chem.* **2025**, *97* (26), 13984−13992.
(47) Chen, F.-Z.; Hou, L.; Gao, Y.; Zhou, J.-Y.; Kong, F.-Y.; Han, D.-M.; Zhao, W.-W. Polyoxometalates: Cascading Functionality to Unique On-Off Organic Photoelectrochemical Transistor Operation. *Adv. Funct. Mater.* **2024**, *34* (48), No. 2408186.
(48) Yu, Z.; Xu, Z.; Zeng, R.; Xu, M.; Zou, M.; Huang, D.; Weng, Z.; Tang, D. Tailored Metal−Organic Framework-Based Nanozymes for Enhanced Enzyme-Like Catalysis. *Angew. Chem., Int. Ed.* **2025**, *64* (7), No. e202420200.
(49) Yu, Z.; Xu, Z.; Zeng, R.; Xu, M.; Zheng, H.; Huang, D.; Weng, Z.; Tang, D. D-Band-Center-Engineered Platinum-Based Nanozyme for Personalized Pharmacovigilance. *Angew. Chem., Int. Ed.* **2025**, *64* (2), No. e202414625.

https://doi.org/10.1021/acs.analchem.6c03166
Anal. Chem. 2026, 98, 19314−19322